Inorganic Chemistry

Article

pubs.acs.org/IC

Photophysical Properties of Cyclometalated Pt(II) Complexes: Counterintuitive Blue Shift in Emission with an Expanded Ligand π System

Alberto Bossi,[†,‡] Andreas F. Rausch,[§] Markus J. Leitl,[§] Rafał Czerwieniec,[§] Matthew T. Whited,[†] Peter I. Djurovich,[†] Hartmut Yersin,*[,§] and Mark E. Thompson*[,†]

[†]Department of Chemistry, University of Southern California, Los Angeles, California 90089, United States

[‡]Dipartimento di Chimica Organica e Industriale, Università degli Studi di Milano, via Venezian 21, 20133 Milano, Italy

[§]Institut für Physikalische Chemie, Universität Regensburg, D-93040 Regensburg, Germany

Supporting Information

ABSTRACT: A detailed examination was performed on photophysical properties of phosphorescent cyclometalated (C^N)Pt(O^O) complexes (ppy)Pt(dpm) (**1**), (ppy)Pt(acac) (**1′**), and (bzq)Pt(dpm) (**2**) and newly synthesized (dbq)Pt(dpm) (**3**) (C^N = 2-phenylpyridine (ppy), benzo[*h*]quinoline (bzq), dibenzo[*f*,*h*]-quinoline (dbq); O^O = dipivolylmethanoate (dpm), acetylacetonate (acac)). Compounds **1**, **1′**, **2**, and **3** were further characterized by single crystal X-ray diffraction. Structural changes brought about by cyclometalation were determined by comparison with X-ray data from model C^N ligand precursors. The compounds emit from metal-perturbed, ligand-centered triplet states (E_{0-0} = 479 nm, **1**; E_{0-0} = 495 nm, **2**; E_{0-0} = 470 nm, **3**) with disparate radiative rate constants ($k_r = 1.4 \times 10^5$ s^{-1}, **1**; $k_r = 0.10 \times 10^5$ s^{-1}, **2**; $k_r = 2.6 \times 10^5$ s^{-1}, **3**). Zero-field splittings of the triplet states (ΔE_{III-I} = 11.5 cm^{-1}, **1′**; ΔE_{III-I} < 2 cm^{-1}, **2**; ΔE_{III-I} = 46.5 cm^{-1}, **3**) were determined using high resolution spectra recorded in Shpol'skii matrices. The fact that the E_{0-0} energies do not correspond to the extent of π-conjugation in the aromatic C^N ligand is rationalized on the basis of structural distortions that occur upon cyclometalation using data from single crystal X-ray analyses of the complexes and ligand precursors along with the triplet state properties evaluated using theoretical calculations. The wide variation in the radiative rate constants and zero-field splittings is also explained on the basis of how changes in the electronic spin density in the C^N ligands in the triplet state alter the spin−orbit coupling in the complexes.

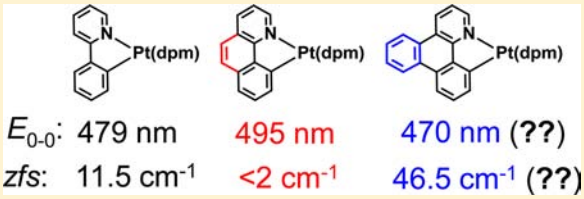

1. INTRODUCTION

Luminescent square planar platinum complexes have been used in numerous photonic applications.[1−6] These materials have especially attracted a great deal of attention for their phosphorescent properties as the heavy metal center enables effective intersystem crossing to the triplet state. Cyclometalated Pt complexes in particular have been extensively studied for use as phosphorescent emitters in organic light-emitting diodes (OLEDs) since they enable all electrogenerated singlet and triplet excitons to be used for light emission.[7−15] Understanding the electronic structures and excited states of these emitters is thus important in order to apply this knowledge to practical applications.

The photophysical properties of Pt(II) compounds, as well as those of other heavy transition metal complexes, incorporating Ir(III), Os(II), Ru(II), etc. strongly depend on the chemical structures of the cyclometalated (C^N) ligands.[16,17] In this regard, the emission energies of cyclometalated Pt(II)(β-diketonate) complexes have been shown to be intimately related to the nature of the chromophoric C^N ligand. Considering (ppy)Pt(dpm) (**1**; Chart 1; ppy = 2-phenylpyridyl, dpm = dipivolylmethanoate) as a reference compound, phosphorescence from this complex (E_{0-0} = 479 nm) has been assigned to a ligand-centered triplet state (^{3}LC) that is strongly perturbed by admixtures with higher-lying metal-to-ligand charge transfer (MLCT) states.[18,19] The energy of this triplet state can be tailored by modifications of the ppy backbone at either the phenyl or the pyridine ring. For example, introducing fluorine atoms to the 4′,6′ positions (Chart 1) of the phenyl ring leads to a hypsochromic shift that can be further augmented by adding donor groups (e.g., methoxy or dimethylammino groups) to the 4 position of the pyridine ring, e.g. (4′,6′-F$_2$-4-OCH$_3$-ppy)Pt(dpm), E_{0-0} = 438 nm.[19] Conversely, adding electron donating groups to the phenyl ring generally causes a bathochromic shift in emission, e.g. (4′-OCH$_3$-ppy)Pt(dpm), E_{0-0} = 525 nm.[19] These spectral shifts are often attributed to the destabilization (or stabilization) of the higher lying ^{1}MLCT state (relative to **1**) caused by increasing (or decreasing) the energy of the HOMO−LUMO gap. Other modifications of the cyclometalating ligand also lead to large changes in the phosphorescent energy. In particular, extending the π-conjugation of the C^N ligand (either on the phenyl or on the pyridine ring) has been shown to red shift the emission,

Received: May 19, 2013
Published: October 11, 2013

Chart 1. Structures of the Studied (C^N)Pt(dpm) Compounds

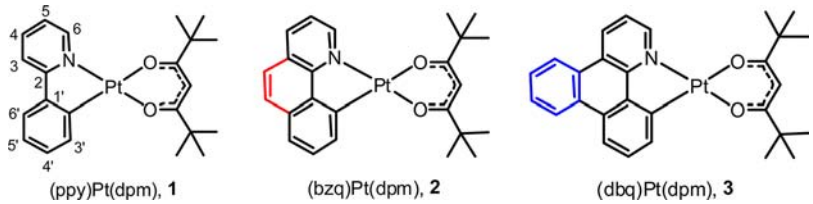

e.g., (2-phenylquinolyl-$N,C^{2'}$)Pt(dpm), E_{0-0} = 550 nm.[17,19] However, sole focus on the HOMO and LUMO energies cannot account for effects on singlet−triplet splittings or differences in the radiative rate constants of emission. For example, another complex with an extended π-system, (bzq)Pt(dpm) (**2**; bzq = benzo[*h*]quinolinyl, E_{0-0} = 495 nm), has an emission lifetime of τ = 125 μs at T = 77 K that is over an order of magnitude longer than that of **1** (τ = 9 μs).[19−21] Such large variations in luminescent lifetime are intimately related to spin−orbit coupling (SOC) interactions between the ^{3}LC and perturbing MLCT states. Therefore, elucidating the phosphorescent properties of these complexes, and related Ir(III) derivatives, requires a detailed understanding of the electronic properties of both the cyclometalating ligand and its interaction with the metal center.

In this paper, we report the synthesis of a cyclometalated Pt(II) compound, (dbq)Pt(dpm) (**3**, dbq = dibenzo[*f,h*]-quinolinyl), which has an expanded π-system that is larger than the one of either **1** or **2** yet gives blue-shifted phosphorescence. The same trend is observed in the triplet energies of the free ligands, i.e., dbqH > ppyH > bzqH,[22−24] as well as for the related hydrocarbons, triphenylene > biphenyl > phenanthrene.[25] The photophysical properties of the complexes, and the somewhat surprising blue shift observed for **3**, will be explained on the basis of their electrochemical properties, X-ray structures, results from DFT calculations, and especially detailed photophysical studies, including high-resolution investigations at cryogenic temperatures. The blue-shifted emission and high radiative rate constant for **3** makes it an interesting candidate for use as a phosphorescent dopant in OLEDs.

2. EXPERIMENTAL SECTION

Materials and Synthesis. *General Procedure.* The ligand dbqH was purchased from Aldrich and purified by sublimation prior to use. The platinum complexes **1** (and its corresponding acac derivative, (ppy)Pt(acac), **1′**) and **2** were prepared according to literature procedures[19,26] and confirmed by NMR spectroscopy. Compound **3** and its acac derivative, (dbq)Pt(acac) (**3′**), were likewise synthesized according to literature procedures (Scheme 1).[19,26] This involves heating the K_2PtCl_4 salt with 2−2.5 equiv of the dbqH ligand in a 3:1 mixture of 2-ethoxyethanol (Aldrich) and water at 80 °C for 16 h. The isolated monomer and dimer intermediates were precipitated from water and were subsequently reacted with 3 equiv of the chelating diketone and 10 equiv of Na_2CO_3 in 2-ethoxyethanol at 100 °C for 16 h. The solvent was removed under reduced pressure, and the compound was purified by flash chromatography using dichloromethane. Due to the lower solubility of **3′** as compared to **3** and its very similar photophysical properties, the main analysis discussions in this work are focused on **3**.

Scheme 1. Synthetic Procedure for 3 and 3′[a]

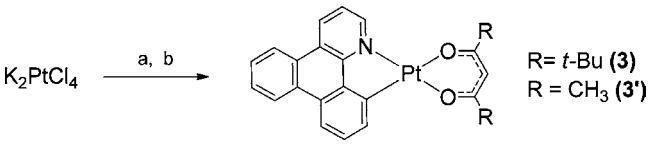

[a](a) 1 equiv K_2PtCl_4, 2.5 equiv of dbqH, 2-ethoxyethanol/water (3:1), 80 °C, 16 h. (b) 3 equiv of 2,2,6,6 tetramethyl 3,5 heptanedione (or 2,4-pentanedione), 10 equiv of Na_2CO_3; 2-ethoxyethanol at 100 °C for 16 h.

Characterization. (dbq)Pt(dpm), **3**: platinum(II) (dibenzo[*f,h*]-quinolinato-N,C^{12}) (2,2,6,6-tetramethyl-3,5-heptadienoato-O,O). Yield: 48%. ^{1}H NMR (ppm, $CDCl_3$, 400 MHz): 1.33 (9H, s); 1.34 (9H, s), 5.87 (1H, s); 7.52 (1H, dd, J = 8.1, 5.6 Hz); 7.61 (1H, dd, J = 8.1, 7.5 Hz); 7.68 (1H, dt, J = 8.1, 1.3 Hz); 7.74 (1H, dt, J = 8.1, 1.3 Hz); 7.84 (1H, d, J = 7.2 Hz); 8.19 (1H, d, J = 7.8 Hz); 8.55 (1H, dd, J = 8.1, 1.1 Hz); 8.66 (1H, dd, J = 8.1, 1.3 Hz); 8.90 (1H, dd, J = 8.1, 1.1 Hz); 9.19 (1H, dd, J = 5.4, 1.1 Hz). LCMS: Retention time, 10.3 min. ESI$^+$ (m/z): 505.2 [M − dpm + 2AcCN]$^+$; 607.3 [M + H]$^+$; 664.3 [M + OH + AcCN]$^+$; 1213.4 [2M + H]$^+$. Anal. calcd for $C_{28}H_{29}NO_2Pt$: C, 55.44; H, 4.82; N, 2.31. Found: C, 55.60; H, 4.63; N, 2.45.

Spectroscopy. UV−visible absorption spectra were measured on a Hewlett-Packard 8453 diode array spectrophotometer. Steady-state emission spectra were measured using a Photon Technology International QuantaMaster model C-60 spectrofluorimeter. Phosphorescence lifetime measurements (>20 μs) were performed using the same fluorimeter equipped with a microsecond xenon flash lamp or obtained using an IBH Fluorocube fluorimeter (<20 μs), equipped with a blue-emitting LED (405 nm) by time-correlated single-photon counting. Luminescent quantum efficiencies (QE) were measured using a Hamamatsu C9920 system equipped with a xenon lamp, a calibrated integrating sphere, and a C10027 photonic multichannel analyzer. The QE measurements were carried out at room temperature in toluene, 2-methyltetrahydrofuran (2-MeTHF), and cyclohexane solutions, respectively, that were deaerated by vigorous bubbling with N_2. Measurements at 77 K were carried out in 2-MeTHF frozen glass since the complexes tend to aggregate at higher concentrations and at low temperatures in the nonpolar solvents methylcyclohexane or 2-methylpentane. Experiments at cryogenic temperatures were carried out in a He cryostat (Cryovac Konti Cryostat IT) in which the He gas flow, He pressure, and heating were controlled. For temperature-dependent lifetime measurements, the third harmonic at 355 nm (28170 cm^{-1}, pulse width <8 ns) of a Nd:YAG laser (IB Laser Inc., DiNY pQ 02) was used. For selectively excited emission and excitation spectra, a pulsed dye laser (Lambdaphysik Scanmate 2C) was operated. The spectra were recorded with an intensified CCD camera (Princeton PIMAX) or a cooled photomultiplier (RCA C7164R) attached to a triple spectrograph (S&I Trivista TR 555). Decay times were registered using a FAST Comtec multichannel scaler PCI card with a time resolution of 250 ps. NMR spectra were recorded on Varian 400 MHz instruments and referenced to residual protons in the solvent. Elemental analyses (CHN) were performed at the Microanalysis Laboratory at the University of Illinois, Urbana−Champaign.

HPLC-MS. HPLC analysis was performed on a Shimadzu Prominance-LCMS 2020 equipped with a column oven (T = 40 °C), a PDA photodetector (200−800 nm), and an MS spectrometer (LCMS 2020; m/z range, 0−2000; ionization modes, ESI/APCI). The ESI/APCI conditions were as follows: nitrogen gas pressure, 100 psi; nitrogen gas flow rate, 1.5 L/min; auxiliary nitrogen gas flow rates, 15 L/min; interface voltage, −3.5 kV; interface current, 0.1 μA; corona needle voltage, −3.5 kV; corona needle current, 0.1 μA; dissolvation

dx.doi.org/10.1021/ic4011532 | Inorg. Chem. 2013, 52, 12403−12415

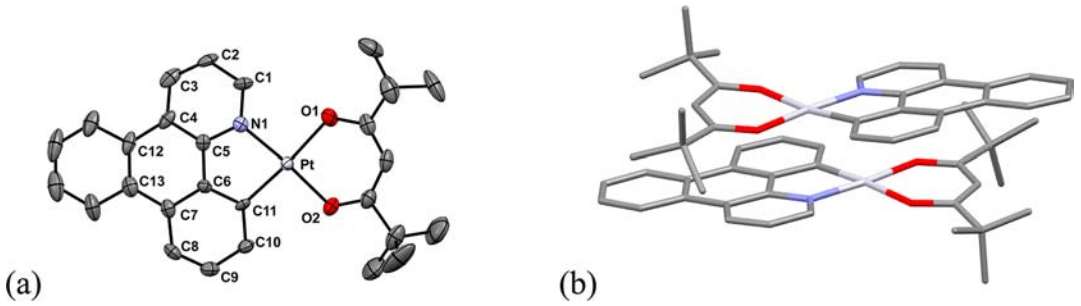

Figure 1. (a) Perspective view of **3** with hydrogen atoms omitted for clarity. (b) Head to tail arrangement of dimer.

Table 1. Selected Bond Lengths (Å) for the Complexes 1, 1′, 2, and 3 and the Ligands N^CH^NH$^+$, bzqH$_2^+$, and dbqH[a]

bond (Å)	1	1′	2	3	N^CH^NH$^+$[b]	bzqH$_2^+$[c]	dbqH[d]
Pt−C11	1.961(7), 1.961(7)	1.947(8)	1.990(4)	1.999(7), 1.989(7)			
Pt−N1	1.981(5), 1.984(6)	1.979(6)	1.983(4)	1.996(7), 2.001(8)			
Pt−O1	2.068(5), 2.053(5)	2.065(6)	2.032(3)	2.072(6), 2.088(6)			
Pt−O2	1.992(5), 2.007(5)	2.008(5)	2.029(3)	2.010(7), 2.002(5)			
C5−C6	1.458(10), 1.460(11)	1.448(12)	1.428(6)	1.421(11), 1.425(11)	1.477(4)	1.432(5)	1.464(2)
C4−C12			1.436(7)	1.474(13), 1.501(11)		1.430(5)	1.459(2)
C7−C13			1.439(7)	1.450(12), 1.462(12)		1.428(6)	1.462(2)
C12−C13			1.353(7)	1.400(14), 1.407(13)		1.347(6)	1.408(2)

[a]For convenience, atom numbering for **1**, **1′**, and **2** follows the scheme used for **3** in Figure 1a. [b]Ref 42. [c]Ref 43. [d]Ref 44.

line (DL) voltage, 0 V; DL temperature, 250 °C; heat block temperature, 400 °C; Q-array RF voltage, 14.6 V; detector voltage, 0.95 V; IG vacuum, 7×10^{-4} Pa. HPLC was performed using a 90:10 mixture of acetonitrile and water (0.3 mL/min) on an Inertsil C8−3 C8 5 mm, 3 × 150 mm.

Electrochemistry. Cyclic voltammetry and differential pulsed voltammetry were performed using a PAR Versastat 3-200 potentiostat/galvanostat. Anhydrous DMF (Aldrich) was used as the solvent under an inert atmosphere, and 0.1 M tetra(*n*-butyl)-ammonium hexafluorophosphate ($TBAPF_6$) was used as the supporting electrolyte. A glassy carbon disk was used as the working electrode. A platinum wire was used as the counterelectrode, and a silver wire was used as a pseudo-reference electrode. The redox potentials are based on values measured from differential pulse voltammetry and are reported relative to a ferrocenium/ferrocene (Cp_2Fe^+/Cp_2Fe) redox couple used as an internal reference,[27,28] while electrochemical reversibility was determined using cyclic voltammetry

Theoretical Calculations. Density functional theory (DFT) calculations for the ligands and complexes were performed using the Titan software package (Wavefunction, Inc.) at the B3LYP/LACVP** level, and TD-DFT calculations were performed using the Gaussian 03 package.[29] The 10 lowest singlet and triplet transitions have been calculated by TD-DFT at the B3LYP/LAN2DZ level for the ground state geometry. The singlet geometries were used to calculate single point triplet molecular orbitals. Kohn−Sham orbitals were rendered with Titan computational package for the frontier orbital surfaces and the spin densities of the triplet states.

X-Ray Crystallography. Diffraction data for compounds **1**, **1′**, **2**, and **3** were collected at room temperature (T = 23 °C) on a Bruker SMART APEX CCD diffractometer with graphite monochromated Mo Ka radiation (λ = 0.71073 Å). The cell parameters for the Pt complexes were obtained from the least-squares refinement of the spots (from 60 collected frames) using the SMART program.[30] A hemisphere of the crystal data was collected up to a resolution of 0.75 Å. The intensity data were processed using the SAINT[31] (for **1**, **1′**, and **3**) and SAINT-Plus[32] (for **2**) programs. All calculations for structure determination were carried out using the SHELXTL package (versions 5.10[33] and 6.12[34]). Initial atomic positions were located with Patterson methods using XS, and structure was refined with least-squares methods using the SHELXL-97[35,36] (for **1**, **1′**, and **3**) and SHELXL-2012-4[37] (for **2**) software packages. Absorption corrections were applied by using SADABS.[38,39] Calculated hydrogen positions were input and refined in a riding manner along with the attached carbons.

3. RESULTS AND DISCUSSION

3.1. Syntheses and Crystal Structures. The new compound **3** was synthesized from dbqH, 2,2,6,6-tetramethyl-3,5-heptanedione (dpmH), and K_2PtCl_4 according to a conventional procedure (Scheme 1).[19] The analogous compound **3′** with a 2,4-pentanedionato (acac) ligand was also prepared and found to have similar absorption and emission properties (see the Supporting Information, Figure 2). However, all further characterization was performed on the more soluble dpm derivative.

Single crystals of **1**, **1′**, **2**, and **3** were grown from DCM/MeOH solution and characterized using X-ray crystallography. The structure of **3** is shown in Figure 1 while those of 1′, 1, and 2 are shown in Figures S4−S6 and Table 1 lists selected bond lengths for all the complexes, along with data of their free C^N ligands (or analogs) taken from the literature. There are two unique molecules in the unit cells of complexes **1** and **3** as opposed to only one in **1′** and **2**. Head-to-tail dimers are present in **1**, **1′**, and **3** separated by mean planes that are 3.3−3.5 Å apart. The shortest intermolecular contact is Pt···C4 = 3.26 Å in **3**; however, there are no close interactions between the two Pt centers within the dimers as the nearest Pt···Pt distance is 3.67 Å in **1′**. The range of Pt−C distances in **1**, **1′**, **2**, and **3** (1.947(8)−1.999(7) Å) straddles the mean Pt−C bond length reported for *cis*-Pt(ppy)$_2$ (1.984(4) Å).[40] The Pt−N distances (1.979(6)−2.001(8) Å) also fall within values reported for related cyclometalated Pt(*β*-diketonate) derivatives, as do the values for the Pt−O1 and Pt−O2 distances.[19,41] The coordination geometry in all the derivatives is distorted square planar because the C−Pt−N bond angles range between 81.3(3)° and 82.72(16)°, while the O−Pt−O bond angles range from 90.90(2)° to 92.8(2)°. The coordination environment is near flat; the largest tilt angle between the C11−Pt−N1 and O1−Pt−O2 planes is 5.71° in **3**.

dx.doi.org/10.1021/ic4011532 | *Inorg. Chem.* 2013, 52, 12403−12415

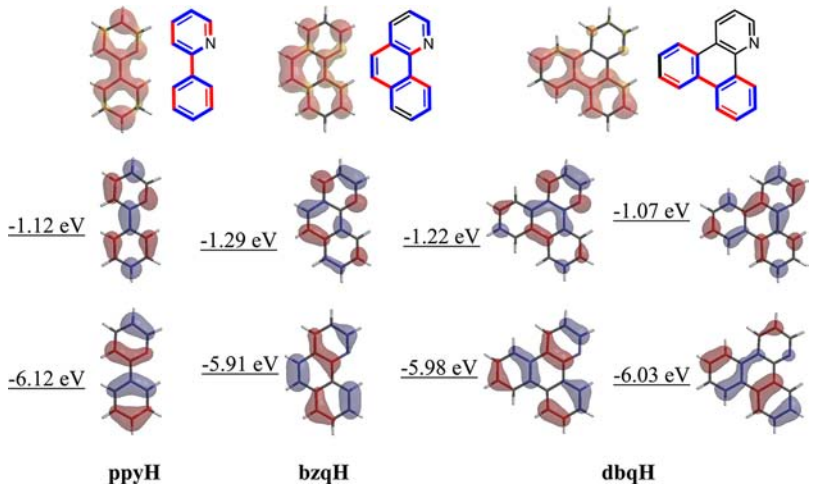

Figure 2. Contour plots for the occupied (HOMO, bottom) and unoccupied (LUMO, middle) frontier orbitals calculated for ppyH, bzqH, and dbqH in the singlet state, along with spin density contours for the triplet state (top). Two pairs of near degenerate frontier orbitals are shown for dbqH. Characteristic changes in bond lengths for the triplet state are also illustrated (decrease, red; increase, blue).

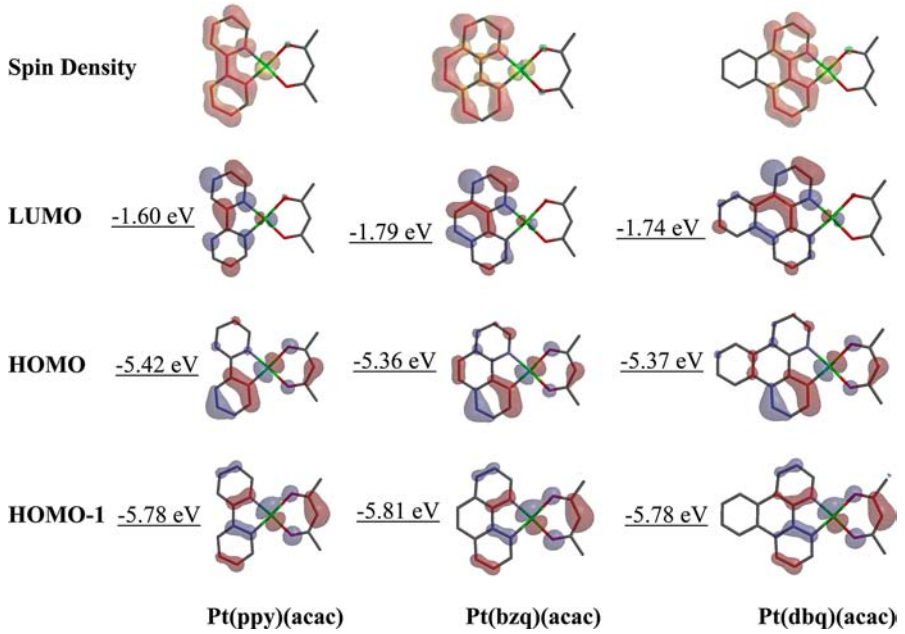

Figure 3. Contour plots for the occupied (bottom, middle) and unoccupied (top middle) frontier orbitals calculated for **1**′, **2**′, and **3**′ calculated in the singlet ground state geometry, along with spin density contours for the triplet state (top).

It is worthwhile to identify any changes in characteristic bond lengths of the C^N ligand that occur upon cyclometalation. While there are no available crystal data on ppyH and bzqH for direct comparison to **1**, **1**′, and **2**, structural data for noncoordinated, protonated 1,3-bis(2-pyridyl)benzene (N^CH^NH$^+$) and bzqH$_2^+$ have been reported.[42,43] An X-ray structure analysis of the free ligand (dbqH) has also been previously reported,[44] and metric data from that study can be used for comparison with the values obtained for complex **3**. Upon coordination of the C^N ligand in **1**, **1**′, and **2**, there is little change in the C5−C6 inter-ring distance (1.477(4) Å in N^CH^NH$^+$, 1.458(10) Å in **1**, 1.448(12) Å in **1**′; 1.432(5) Å in bzqH$_2^+$, 1.428(6) Å in **2**). Likewise, in **3** most of the bond lengths in dbq do not change significantly after cyclometalation. However, variation does occur in the C5−C6 and C4−C12 distances as the former bond is significantly shorter (1.421(11) Å and 1.425(11) Å in **3** versus (1.464(2) Å in dbqH), whereas the latter bond is longer (1.474(13) Å and 1.501(11) Å in **3** versus 1.459(2) Å in dbqH; see Table 1). The change in bond distance suggests that a more localized "ppy-like" electronic configuration is stabilized in the dbq ligand system after cyclometalation.

3.2. Electrochemistry. The redox potentials of the complexes were examined using cyclic voltammetry and differential pulse voltammetry. The reduction potential for complex **1** ($E_{1/2}$ = −2.41 V, reversible)[19] is more cathodic than that found in either **2** ($E_{1/2}$ = −2.16 V, irreversible)[19] or **3** ($E_{1/2}$ = −2.18 V, quasireversible). In analogy with related cyclometalated Pt(II) systems,[45] reduction is considered to involve an orbital that is localized on the C^N ligand. The less negative potentials of **2** and **3** can be attributed to the expanded π-system on the cyclometalated bzq and dbq ligands, which enable these complexes to better accommodate a negative charge than does **1**. The complexes also undergo irreversible

dx.doi.org/10.1021/ic4011532 | *Inorg. Chem.* 2013, 52, 12403−12415

oxidations at $E_{1/2}$ = +0.79 V (**1**), +0.56 V (**2**), and +0.48 V (**3**). As previously reported for related derivatives,[45] oxidation involves a HOMO that is largely localized on the Pt center (oxidized to Pt(III)).[46,47] The irreversible character of the electrochemical processes, particularly upon oxidation, makes it problematic to use the redox data to assess the HOMO−LUMO separation. However, the redox values observed for complexes **2** and **3** relative to **1** are consistent with expectations that expanding the aromatic π-system will lead to a decrease in the HOMO−LUMO gap.

3.3. Theoretical Calculations. Theoretical examination of the frontier orbitals is particularly useful for understanding trends observed in the electrochemical and photophysical properties of molecular materials. Thus, density functional theory (DFT) calculations were performed to gain additional understanding of the electronic structure of the free ligands and the acac analogs of the platinum complexes (**1′**, **2′**, and **3′**). Geometry optimizations of singlet and triplet states were performed using Titan (Wavefunction, Inc.) software, and TD-DFT calculations of the excited states were carried out using Gaussian 03 software. Figures 2 and 3 display the frontier Kohn−Sham orbitals as well as triplet spin density surfaces for the C^N ligands and Pt complexes. Molecular parameters (bond lengths and angles) calculated for the ligands and complexes closely match the experimental X-ray data; likewise TD-DFT calculations on the optimized ground state singlet geometry show good agreement between the predicted absorption energies and oscillator strengths and those observed experimentally. The adiabatic energy of the triplet state was also evaluated by comparing differences in the calculated singlet and triplet state energies (ΔSCF).[48,49] A close correspondence between theory and experiment (*vida infra*) gives us confidence in using theoretical data to understand the excited state behavior of these complexes.

To a first approximation, the electronic structure of the triplet states for ppyH and bzqH can be modeled using a combination of HOMOs and LUMOs, where each orbital contains an unpaired electron.[48,50] Bond length changes occur that correlate with diminished bonding interactions in the HOMO and enhanced bonding interactions in the LUMO according to a HOMO−LUMO excitation. For ppyH, these changes lead to a quinoidal electron distribution that is accompanied by a characteristic decrease in bond length between the aromatic rings (1.492 Å for S_0, 1.395 Å for T_1).[50] In contrast, the structure for the T_1 state of bzqH distorts in a manner similar to that of stilbenes,[48] as the separation between carbon atoms of the ethene bridge increases (1.362 Å for S_0, 1.492 Å for T_1) whereas the distances of the bonds connecting the ethene bridge to the aromatic rings decrease (1.437 Å for S_0, 1.389 Å for T_1). There is also an *increase* in the separation between aromatic rings (1.453 Å for S_0, 1.487 Å for T_1). These structural changes in bzqH can be viewed as a consequence of a decrease in the aromaticity of the cyclic π-system while in the T_1 state as described by Baird.[51] The change in bond lengths leads to an electronic distribution that places a significant amount of electron (spin) density (40.1%) onto the atoms of the ethene bridge. Destabilization of the HOMO and stabilization of the LUMO, relative to ppyH, also decreases the HOMO−LUMO gap and is responsible for lowering the T_1 energy (calculated $\Delta(S_0 - T_1)$ = 404 nm for ppyH, 447 nm for bzqH).

The picture for the triplet state of dbqH is somewhat more complicated due to the pseudo-D_{3h} symmetry imposed by the parent triphenylene π-system. For this molecule, there are two nearly degenerate pairs of frontier orbitals (HOMO−1, HOMO, LUMO, LUMO+1) that need to be considered when describing the electronic structure of the triplet state. This quasi-degeneracy causes the T_1 state to undergo a Jahn−Teller type of distortion that, along with associated changes in bond lengths, localizes the spin density on just two aromatic rings in a pattern similar to that observed for ppyH. This type of distortion also preserves the aromaticity in the pyridyl ring and is thus favored over the stilbenoid-type changes that occur in bzqH. In addition, there is a 0.14 eV increase in the HOMO−LUMO gap of dbqH relative to bzqH. The stabilization of the HOMO and destabilization of the LUMO upon benzannulation of bzqH is brought about by secondary interactions on the frontier orbitals between the bridging ethene and the added butadiene fragment.[52] Thus, the calculated T_1 energy of dbqH ($\Delta(S_0 - T_1)$ = 429 nm) is higher than that of bzqH.

For the three Pt(II) complexes, the LUMO, as suggested in the Electrochemistry section, is localized (or better delocalized) principally over the cyclometalated ligand and decreases in energy as the π-system gets larger. The energies of the LUMO levels decrease with enlargement of the π-system from −1.60 eV for **1′** to −1.79 eV and −1.74 eV for **2′** and **3′**, respectively. This is in a rough agreement with the fact that the reduction potentials determined for **2** and **3** are anodically shifted by about 200 mV relative to **1**. The HOMOs have near identical contours, consisting primarily of electron density on the metalated phenyl ring, β-diketonate, and platinum center. In contrast to the LUMO, the energies of the HOMO are nearly invariant for the three derivatives. Unfortunately, the irreversible nature of the redox processes precludes a quantitative discussion of the experimental trends versus the theoretical HOMO−LUMO gap. However, the calculated HOMO−LUMO gap for the three complexes is qualitatively consistent with the electrochemical data, decreasing on going from **1′** → **2′** ≈ **3′**. The transition energy to the lowest singlet state in **1′** is calculated to be 403.4 nm (f = 0.0242) and comprised of HOMO→LUMO (89.2%) and HOMO−1→LUMO (10.8%) orbitals,[45,53] whereas in **2′** it is at 423.7 nm (f = 0.0326, HOMO→LUMO (91.6%) and HOMO−1→LUMO (8.4%))[45] and in **3′** at 420.6 nm (f = 0.0220, HOMO→LUMO (91.5%) and HOMO-1→LUMO (8.5%)). The energies of the lowest triplet state for **1′** (466.5 nm), **2′** (497.1 nm), and **3′** (468.3 nm) compare favorably to experimental data for the E_{0-0} emission energies (*vida infra*). The ΔSCF energies calculated for **1′** (471.5 nm), **2′** (480.9 nm), and **3′** (469.4 nm) also follow the trends in emission energy.

Bond lengths in the cyclometalated C^N ligand undergo changes in the triplet state that parallel those calculated for the free ligands. The C5−C6 bond distance of **1′** in the S_0 state (calculated, 1.461 Å; experimental, 1.448 (12) Å) significantly decreases to 1.404 Å in the optimized T_1 geometry. Conversely, the C5−C6 bond length in **2′** does not appreciably change in the T_1 state. However, the bridging ethane (C12−C13) bond length increases from 1.369 Å to 1.437 Å, while the C4−C12 and C7−C13 distances contract from 1.440 Å to 1.395 Å. In complex **3′**, the C5−C6 bond contracts, in a manner analogous to that in **1′**, from 1.434 Å in the S_0 state to 1.386 Å in the T_1 state, whereas the bonds connecting the benzannulated ring (C4−C12, C12−C13 and C7−C13) are essentially unperturbed (≤0.003 Å change).

dx.doi.org/10.1021/ic4011532 | *Inorg. Chem.* 2013, 52, 12403−12415

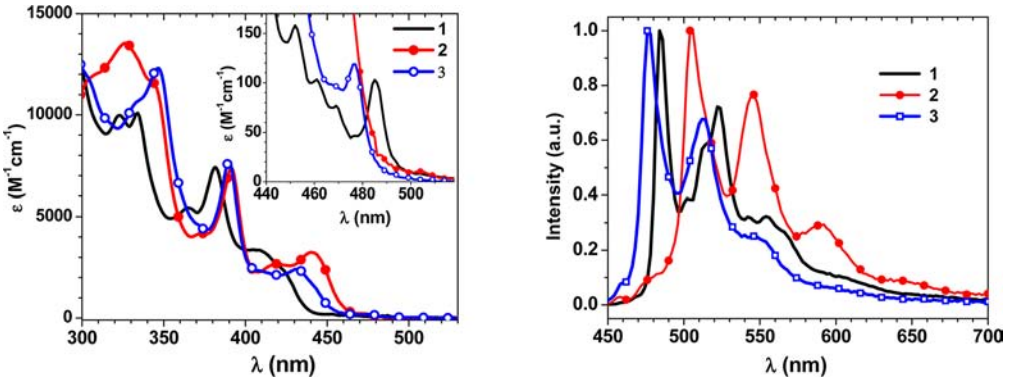

Figure 4. Absorption (left) and emission (right) spectra of (ppy)Pt(dpm) (**1**; (black), (bzq)Pt(dpm) (**2**; red, filled circles), and (dbq)Pt(dpm) (**3**; blue, open circles) in cyclohexane at ambient temperature.

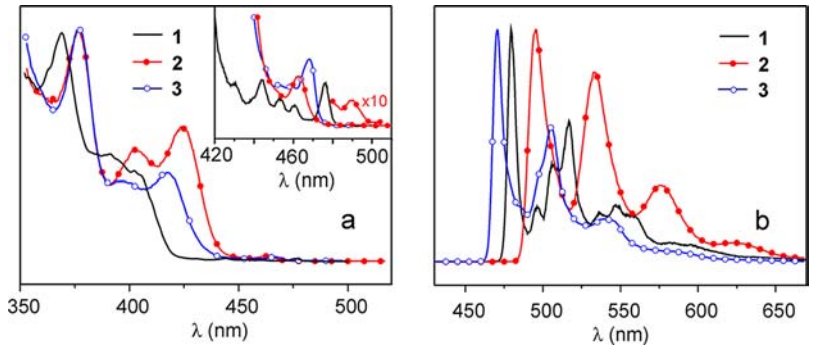

Figure 5. Excitation (a) and emission (b) spectra of (ppy)Pt(dpm) (**1**; black), (bzq)Pt(dpm) (**2**; red, filled circles), and (dbq)Pt(dpm) (**3**; blue, open circles) in 2-MeTHF at 77 K.

Table 2. Emission Properties of the Pt(II) Complexes 1, 2, and 3

	RT[a]						77 K[b]	
complex	λ_{max} (nm)	Φ_{PL}	τ (μs)	k_r (s^{-1})[c]	k_{nr} (s^{-1})[c]	K_{SQ} (M^{-1} s^{-1})[d]	λ_{max} (nm)	τ (μs)
1	485	0.33	2.4	1.4×10^5	2.8×10^5	7.4×10^8	479	8.7
2	505	0.29	29.6	0.10×10^5	0.24×10^5	2.2×10^9	495	125
3	477	0.20	0.76	2.6×10^5	11×10^5	4.0×10^9	470	7.0

[a]In cyclohexane. [b]In 2-MeTHF. [c]$k_r = \Phi_{PL}/\tau$, $k_{nr} = (1 - \Phi_{PL})/\tau$; assuming that the emissive state is populated with unit efficiency. [d]K_{SQ}: the bimolecular self-quenching rate constant determined from the gradient of a plot of τ^{-1} versus concentration. τ and Φ_{PL} were measured under deaerated conditions.

The spin densities of the Pt(II) complexes for the triplet states present electronic structures that differ markedly from the ones derived by only considering the orbital overlap between the HOMO and LUMO of the S_0 state. Instead, there is a close correspondence to contours seen in the T_1 state of the free C^N ligand precursors. The spin distributions also illustrate how differences in the electronic structures of the ligand T_1 states exert their influence on the metal complexes. The spin density of **1**′ is localized primarily on the ppy ligand (86.5%), a significant portion of which is on the nitrogen (10.1%), metalated carbon (14.2%), and two atoms connecting the phenyl and pyridyl rings (21.0%). Most of the remaining spin in the complex resides on Pt (12.2%). This latter value can be used to gauge the ability of Pt to promote spin−orbit coupling in the excited state.[16,54] In **2**′, a majority of the spin density also resides on the bzq ligand (93.0%), although in contrast to **1**′, a significant portion is now shifted onto the peripheral atoms of the bridging ethene bond (23.2%) rather than the carbon atoms linking the pyridyl and metalated aromatic rings (4.3%). This change in electron distribution is accompanied by a sharp decrease in spin density at the nitrogen (4.9%), metalated carbon (3.2%), and, significantly, Pt (5.1%) ion. In the case of **3**′, the spin density does not extend over the entire π-system of the dbq ligand but instead localizes on the metalated phenyl-pyridine moiety (83.0%). The similarity of **1**′ and **3**′ in respect to the triplet state spin distribution is paralleled by similar geometry changes predicted to occur in the T_1 state of both compounds. In particular, the C5−C6 bonds in **1**′ and **3**′ become considerably shorter by 0.06 and 0.05 Å, respectively. Since in **3**′ the triplet state spin density is centered at the cyclometalated part of the dbq ligand, it is concluded that the quinoidal distortion in the excited state of **3**′ preserves the aromaticity and electronically isolates the benzannulated ring from participation in the T_1 state properties. Moreover, the spin densities on atoms connecting the phenyl and pyridyl rings (14.8%), nitrogen (10.9%), the metalated carbon (12.6%), and Pt (12.3%) are comparable to that of **1**′. The similarity in the contours for the spin densities of **1**′ and **3**′, as well as in the bond length alternation, are thus consistent with the close match of T_1 state energies calculated for both species.

dx.doi.org/10.1021/ic4011532 | Inorg. Chem. 2013, 52, 12403−12415

3.4. Photophysical Properties at Ambient Temperature and 77 K. The absorption and emission spectra of **1**,[19,45] **2**,[19,45] and **3** were recorded at ambient temperature in fluid solution (Figure 4), and excitation and emission spectra at 77 K were measured in frozen glass (Figure 5). The luminescence data are compiled in Table 2. The absorption spectra display ligand-centered (LC) $\pi-\pi^*$ transitions between 200 and 350 nm ($\varepsilon > 10^4$ M^{-1} cm^{-1}). These bands are only slightly shifted with respect to the free ligands and are not solvatochromic. A series of weaker bands at lower energy ($\lambda \approx$ 350−460 nm, $\varepsilon < 10^4$ M^{-1} cm^{-1}) is assigned to spin allowed metal-to-ligand charge-transfer (^{1}MLCT) transitions as these features are absent in the spectra of the free ligands. These bands blue-shift with increasing solvent polarity (e.g., for **3**: cyclohexane (λ = 432 nm) < toluene (λ = 420 nm) < CH_2Cl_2 (λ = 411 nm)), which indicates that the corresponding ^{1}MLCT states are less polar than the singlet ground state. Absorption between 450 and 510 nm (Figure 4a, inset) is assigned to the formally forbidden S_0-T_1 transitions that become slightly allowed due to spin−orbit coupling induced by the metal center. There is a significant difference in the molar absorptivity for the S_0-T_1 transitions of **1** (λ_{max} = 485 nm, $\varepsilon \approx$ 100 M^{-1} cm^{-1}) and **3** (λ_{max} = 476 nm $\varepsilon \approx$ 110 M^{-1} cm^{-1}) as compared to **2** ($\lambda_{max} \approx$ 500 nm, $\varepsilon \approx$ 1 M^{-1} cm^{-1}). The lower intensity of the S_0-T_1 transitions of **2** indicates a decreased allowedness relative to that which occurs in **1** and **3**. It is also noteworthy that while the energy of the lowest ^{1}MLCT absorption bands of **3** lie between that of **1** and **2**, the S_0-T_1 absorption transition in **3** is blue-shifted with respect to **1** and **2** (i.e., 476 nm (**3**), 485 nm (**1**), and ∼504 nm (**2**), Figure 4a). Thus, the energy separation between the lowest triplet state T_1 and the closest ^{1}MLCT state(s) is significantly smaller in **3** as compared to **1** and **2**. This behavior may be rationalized by a smaller exchange interaction for **3** as compared to **1** and **2**. The equivalent information is more apparent in comparisons using the better resolved excitation spectra of the compounds recorded at 77 K in 2-MeTHF (Figure 5a). Here the S_0-T_1 transitions are rigidochromically blue-shifted with respect to the ambient temperature absorptions in fluid solutions, lying at 476 nm (**1**), 490 nm (**2**), and 468 nm (**3**). Other weak bands/shoulders in the excitation spectra of **1** and **3** in this low-energy range (inset in Figure 5a) correspond to vibrational satellites of the T_1 state.

The emission spectra at 300 K (Figure 4b) display structured profiles consisting of electronic transitions with maxima at 485 nm (**1**), 505 nm (**2**), and 477 nm (**3**), respectively, and vibrationally induced bands corresponding to ground state modes of the ligands (band spacing ∼1400−1500 cm^{-1}). Luminescent decay times in the microsecond range (τ_{RT}(**1**) = 2.4 μs; τ_{RT}(**2**) = 29.6 μs; τ_{RT}(**3**) = 0.76 μs) show that the emissions originate from triplet states. The excited state distortion, as coarsely estimated by the intensity ratio of the first vibrational satellite band as compared to the electronic origin, is slightly less for **3** (0.68) than for **1** (0.73) and for **2** (0.77), presumably being a consequence of different rigidities of the ligands. In frozen 2-MeTHF glass at 77 K (Figure 5b), the emissions are blue-shifted (λ_{max}(**1**) = 479 nm, λ_{max}(**2**) = 495 nm and λ_{max}(**3**) = 470 nm) as compared to T = 300 K and the decay times increase to τ_{77K}(**1**) = 8.7 μs, τ_{77K}(**2**) = 125 μs, and τ_{77K}(**3**) = 7.0 μs. Thus, compound **3**, despite having a larger π-system, has an emission energy that is higher than either **1** or **2** at ambient temperature and 77 K. *This shift to higher energy is contrary to what is typically observed when luminescent complexes have their π-systems extended with aromatic rings*. However, this trend is predicted by the TD-DFT calculations discussed in section 3.3.

A corresponding situation with respect to the separation between electronic transition energies of the S_1 and T_1 states found in the Pt complexes is also observed in the emission spectra of the free ligands (see Supporting Information, Figure 10). At 77 K, ppyH, bzqH, and dbqH display fluorescence between 320 and 400 nm with the energy of the singlet state of bzqH (345 nm) and dbqH (340 nm) both lower than ppyH (at λ_{max} = 330 nm), as expected for compounds with an expanded π-system. This energetic ordering, however, is not followed for the triplet state as the E_{0-0} peaks for phosphorescence lie at 424 nm (dbqH), 430 nm (ppyH) and 455 nm (bzqH). The higher triplet energy of dbqH relative to ppyH and bzqH has precedence in the T_1 energies of the corresponding polycyclic aromatic hydrocarbons triphenylene (E_{0-0} = 431 nm),[55] biphenyl (E_{0-0} = 435 nm),[56] and phenanthrene (E_{0-0} = 462 nm).[57] Moreover, upon coordination of the C^N ligands to platinum, the T_1 energies are red-shifted by ∼2400 cm^{-1} (49 nm) in **1**, ∼1800 cm^{-1} (40 nm) in **2**, and ∼2300 cm^{-1} (46 nm) in **3**. Therefore, the unexpectedly high T_1 energy of dbqH, together with the slightly smaller red-shift after cyclometalation, is considered to be the main reason for the blue-shifted emission of **3** versus **1**.

Significant differences are also observed in other photophysical properties of the three complexes. The materials undergo self-quenching in solution with rate constants that increase as the π-system gets larger: **1** (K_{SQ} = 0.74 × 10^9 M^{-1} s^{-1}), **2** (K_{SQ} = 2.2 × 10^9 M^{-1} s^{-1}) and **3** (K_{SQ} = 4.0 × 10^9 M^{-1} s^{-1}). The luminescence quantum efficiency in solution decreases in the same order: **1** (Φ = 0.33) > **2** (Φ = 0.29) > **3** (Φ = 0.20). However, the lower efficiency of **3** in solution cannot be attributed to the higher rate constant of self-quenching. The quantum yields and lifetimes do not vary when concentrations are low enough (≤10^{-6} M) to approach infinite dilution. Instead, variations in the quantum yields and decay times are a consequence of differences in the intrinsic nonradiative decay behavior of the materials, being highest for **3** (k_{nr} = 11 × 10^5 s^{-1}) followed by **1** (k_{nr} = 2.8 × 10^5 s^{-1}) and **2** (k_{nr} = 0.24 × 10^5 s^{-1}). The trend does not follow the behavior expected if the rate constants simply followed the energy gap law,[58,59] since the nonradiative rate constants would be expected to increase in the order **3** < **1** < **2** with decreasing emission energy. However, an additional mechanism that can contribute to nonradiative decay in fluid solution is thermal deactivation via a higher energy ligand field (^{3}LF) state.[16,60,61] Considering that the coordination environment around the metal center is nearly identical in all three complexes, similar ligand field strengths of the chromophoric ligands can be assumed. Thus, the lowest ^{3}LF states should be at roughly the same energy for all three species. The activation energy for the thermal population of the quenching states should therefore decrease in the order **2** > **1** > **3** and make nonradiative decay most favorable for the complex with the highest energy T_1 state. This assumption is supported by the fact that the quantum yields of all three complexes increase to about 70% in 2 wt % doped polymethylmethacrylate (PMMA) films. In the rigid environment of PMMA, the tendency of the ^{3}LF states to undergo an energy stabilizing distortion from a square-planar toward a tetrahedral geometry is partly suppressed. The activation energies for the population of the ^{3}LF states thus increase, and consequently, the decreased rate constant for nonradiative decay leads to quantum yields that are significantly

dx.doi.org/10.1021/ic4011532 | Inorg. Chem. 2013, 52, 12403−12415

higher than in fluid solution. Similar models have also been applied to explain the relatively high emission quantum yields of Ru(II) polypyridine compounds in rigid host media like zeolites,[62] glasses,[63] or polymeric matrices[64] when compared to fluid solutions.

A rather pronounced variation in the radiative rate constants for the three complexes is also observed. The formally forbidden transition from the T_1 state to the singlet ground state is distinctly more allowed (higher radiative rate constants) in **3** ($k_r = 2.6 \times 10^5\ s^{-1}$) than in **1** ($k_r = 1.4 \times 10^5\ s^{-1}$) or **2** ($k_r = 0.10 \times 10^5\ s^{-1}$; Table 2). The values for the radiative rate constants roughly follow intensity differences in the molar absorptivity for the lowest energy S_0-T_1 transitions. These large differences cannot be traced back solely to the different emission energies of the compounds, which according to Einstein's law of spontaneous emission predicts an increase of the radiative rate constant with the third power of the emission energy.[65,66] (Compare also eq 2, see below.) More importantly, the observed values indicate differences in the efficiency of spin–orbit coupling (SOC) between the sublevels of the emitting triplet state and higher lying singlet MLCT states.[67] Moreover, SOC also significantly influences the intrinsic vibrationally induced radiationless relaxation of the emitting T_1 state via $T_1 \rightarrow S_0$ intersystem crossing.[65,66] Indeed, it has been recently demonstrated for cyclometalated Ir(III) complexes that an increase in SOC efficiency also can cause an increase of the nonradiative decay rate constant.[16,68]

3.5. High-Resolution Optical Spectroscopy and Electronic Structures of the Triplet States. The presented spectroscopic investigations of the platinum(II) compounds **1**, **2**, and **3** indicate that the radiative and nonradiative properties of the materials are strongly affected by distinctly different efficiencies of spin–orbit coupling. However, a more detailed understanding of these influences is not possible on the basis of broad and unresolved spectra as measured at ambient temperature or at 77 K. We therefore decided to investigate the materials with methods of high-resolution optical spectroscopy at cryogenic temperatures. In particular, these studies will allow us to determine the energy splittings of the emitting triplet state into substates (zero-field splitting, ZFS). The magnitude of the total splitting ΔE(ZFS) represents a useful parameter for an assignment of the nature of the T_1 state. Moreover, it is possible to gain insight into the effects of SOC between the T_1 state (or more exactly its substates) and higher lying states.[11,16,67,69,70]

For the studies at liquid helium temperatures, the compounds were dissolved in *n*-alkanes at a low concentration of $\sim 10^{-5}$ M and rapidly cooled. In the polycrystalline alkane matrices, the guest molecules (dopants) substitute host molecules and thus lie at defined positions. In suitable cases, the application of this so-called Shpol'skii technique[71] results in highly resolved spectra with line widths of only a few cm^{-1}.[67,69,72–74] These line widths are by a factor on the order of a hundred smaller than those usually obtained with amorphous or glassy host materials.

As a representative example, Figure 6 shows emission spectra of (dbq)Pt(dpm) (**3**) in *n*-hexane at various temperatures. The ambient temperature spectrum largely corresponds to the one measured in cyclohexane as depicted in Figure 4 (right) and discussed above. At 77 K, the emission bands display only slightly smaller half-widths, while at 4.2 K using nonselective excitation, a manifold of highly resolved lines with half-widths of a few cm^{-1} is observed. The spectrum corresponds to a

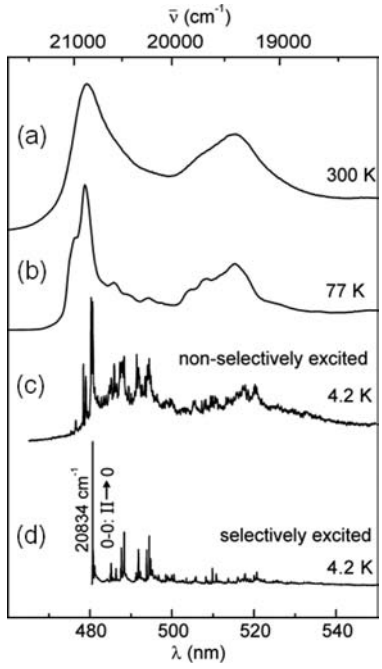

Figure 6. Emission spectra of (dbq)Pt(dpm) (**3**) in *n*-hexane at various temperatures. Excitation wavelengths: (a and b) λ_{exc} = 430 nm, (c) λ_{exc} = 375 nm (nonselective excitation), (d) λ_{exc} = 479.05 nm (selective excitation of one specific site).

superposition of spectra stemming from several sites, representing dopant molecules with slightly different local environments in the polycrystalline host. Using a tunable dye laser, one specific site can be excited selectively. Thus, contributions from other sites and the intensity of the inhomogeneous background are strongly reduced (Figure 6d). It will be shown below that the most intense line in the selectively excited emission of **3** at 4.2 K mainly represents the electronic 0–0 transition from one of the three substates of the emitting triplet state T_1, denoted as substate II, to the singlet ground state S_0 (line at 20 834 cm^{-1}). The lines of minor intensity at lower energies correspond to vibrational satellites stemming from ground state modes.

Subsequently, we will focus on a comparison of the purely electronic properties of the three studied Pt(II) compounds, i.e. on the electronic 0–0 transitions between the T_1 substates and the S_0 ground state. Since for (ppy)Pt(dpm) (**1**) no high resolution spectra of sufficient quality could be obtained, the acac analog **1′**, differing only in the alkyl groups of the nonchromophoric ancillary ligand, was investigated. This approach seems to be justified, since (ppy)Pt(dpm) (**1**) and (ppy)Pt(acac) (**1′**) show very similar photophysical properties at ambient temperature and at 77 K.[19] Moreover, high-resolution spectroscopic studies of the bis-fluorinated analogs of **1** and **1′**, (4,6-dFppy)Pt(dpm) and (4,6-dFppy)Pt(acac), have shown that this similarity also exists at cryogenic temperatures.[75]

Figure 7 shows site selective excitation and emission spectra of (ppy)Pt(acac) (**1′**) and (bzq)Pt(dpm) (**2**) in *n*-octane and (dbq)Pt(dpm) (**3**) in *n*-hexane in the range of the electronic 0–0 transitions at different temperatures. Compound **1′** allows us to observe all three T_1 substates in the excitation spectrum. The transition from the singlet ground S_0 state to the lowest substate I is very weak, while the transitions to the higher lying substates II and III are significantly more intense, showing that

dx.doi.org/10.1021/ic4011532 | Inorg. Chem. 2013, 52, 12403–12415

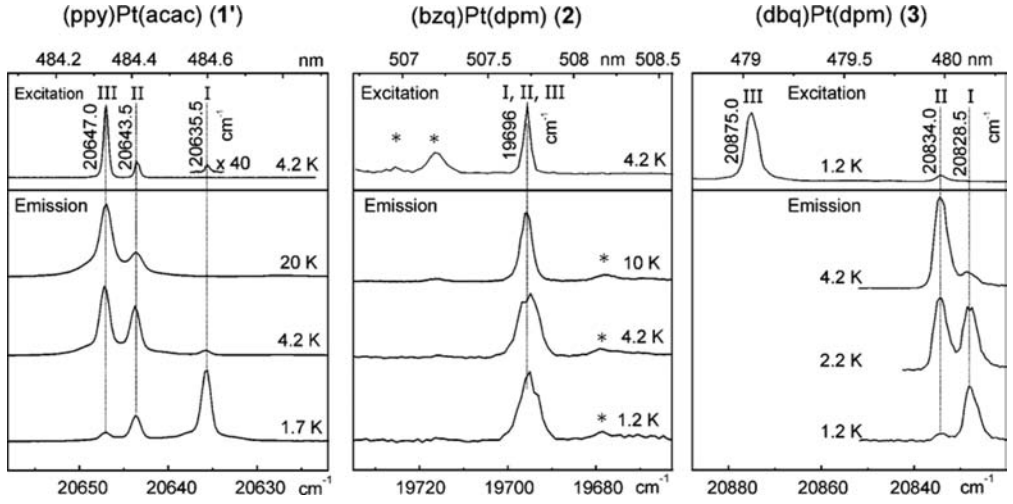

Figure 7. Site selective excitation and emission spectra of (ppy)Pt(acac) (**1**′) and (bzq)Pt(dpm) (**2**) in *n*-octane and (dbq)Pt(dpm) (**3**) in *n*-hexane at different temperatures in the range of the respective electronic 0−0 transitions ($T_1 \leftrightarrow S_0$ transitions). The excitation energies were 21 376 cm^{-1} (**1**′), 20 125 cm^{-1} (**2**), and 20 875 cm^{-1} (**3**), while for the excitation spectra, the emissions were detected at 20 194 cm^{-1} (**1**′), 19 249 cm^{-1} (**2**), and 20 506 cm^{-1} (**3**), respectively. The asterisks displayed in the spectra of **2** refer at the low energy and the high energy side of the 0−0 transitions to phonon satellites and to residual signals of other sites, respectively.[74,77]

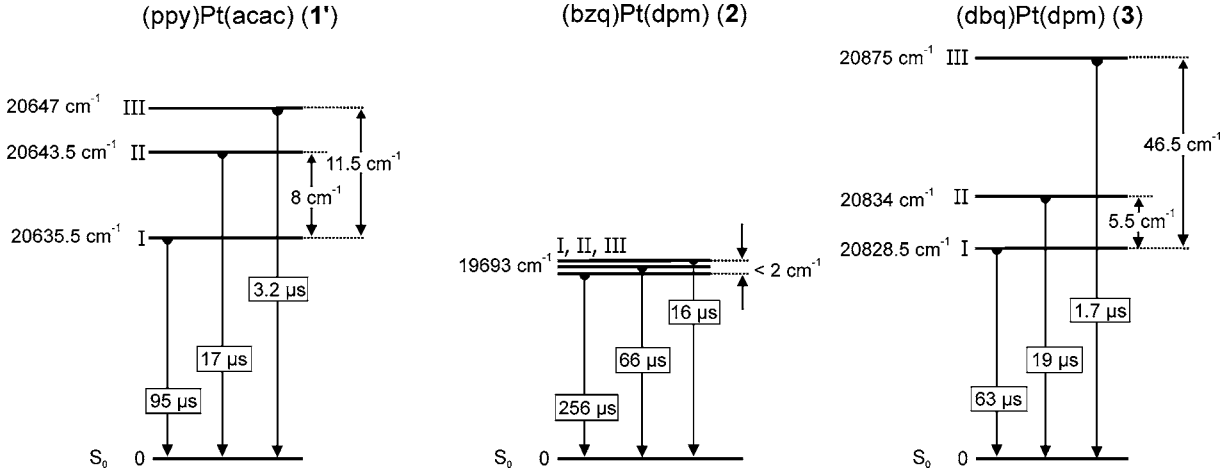

Figure 8. Energy level diagrams of the emitting triplet states and individual substate decay times of (ppy)Pt(acac) (**1**′) and (bzq)Pt(dpm) (**2**) in *n*-octane and (dbq)Pt(dpm) (**3**) in *n*-hexane. The data given for **2** are based on a specific site, which is roughly 10 times as intense as other sites.

they carry distinctly more allowedness. These trends are also manifested in the emission spectra. The 0−0 lines of all three substates are in resonance with their corresponding excitation lines. At temperatures above $T \approx 3$ K, higher lying substates II and III dominate the emission spectra. The zero-field splitting parameters amount to $\Delta E_{II-I} = 8$ cm^{-1} and $\Delta E_{III-I} = \Delta E(ZFS) = 11.5$ cm^{-1}.

In the emission and excitation spectra of (bzq)Pt(dpm) (**2**), only one line at 19 693 cm^{-1} can be observed, being independent of temperature in the investigated range. The weak structures in the excitation and emission spectra lying ∼20 cm^{-1} separated from these electronic 0−0 transitions represent phonon satellites (compare with ref 74). This behavior indicates very small splittings of the three T_1 substates that cannot be resolved with our equipment due to the inhomogenous broadenings of the transitions. Evidence for this assumption can be gained from emission measurements under application of a high magnetic field. Due to the Zeeman effect, the wave functions of close-lying T_1 sublevels significantly mix, which leads to distinct shifts of their 0−0 energies.[74,76] In the case of **2**, a typical Zeeman splitting of 18 cm^{-1} is observed at a field strength of **B** = 10 T, proving that the three T_1 substates lie indeed within the experimental resolution of ∼2 cm^{-1} at zero magnetic field.[77]

In strong contrast, the triplet state splitting of (dbq)Pt(dpm) (**3**) is significantly larger than in **2** or even **1**′. The substates I and II govern the emission behavior at low temperatures. They are separated by 5.5 cm^{-1}, while substate III is observed 46.5 cm^{-1} above substate I. Since the excitation line 0 → III is significantly more intense than the line corresponding to the transition 0 → II, it can be assumed that substate III dominates the emission properties at temperatures significantly higher than $T \approx 4.2$ K. On the other hand, the transition from the singlet ground state to the lowest T_1 substate I is too weak to be observed in the excitation spectrum.

Additional insight into the triplet state properties of the materials can be obtained by temperature dependent measurements of the emission decay time. Such studies are well established in the literature and allow us to determine the individual decay times of the T_1 sublevels (not described in

dx.doi.org/10.1021/ic4011532 | Inorg. Chem. 2013, 52, 12403−12415

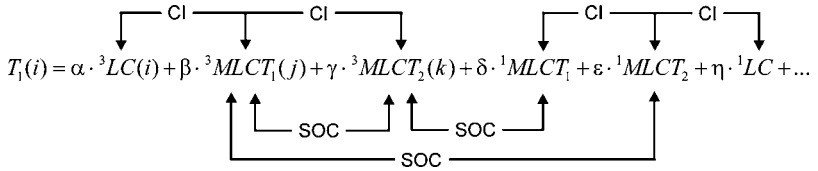

Figure 9. Simplified schematic diagram showing the various spin−orbit coupling (SOC) and configuration interaction (CI) pathways responsible for state mixing in transition metal complexes with ^{3}LC emitting states.

detail here, but compare refs 67, 78−82). The corresponding decay times and the results obtained from the high-resolution measurements as described above are summarized in energy level diagrams depicted in Figure 8. For all three compounds, substate III exhibits the shortest individual decay time, followed by substate II and substate I. This is in accordance with the intensities of the electronic 0−0 transitions observed in the excitation spectra of **1**′ and **3**.

A comparison of the triplet state properties of **1**′, **2**, and **3** allows us to deepen the understanding of the nature of the excited states of the studied compounds. The ΔE_{III-I} splittings, which represent the total zero-field splittings ΔE(ZFS), show distinct differences. According to an empirical ordering scheme,[11,16,67,69,74] the T_1 state of (bzq)Pt(dpm) (**2**) with ΔE(ZFS) < 2 cm^{-1} can be assigned to be largely centered at the chromophoric (bzq) ligand. For (ppy)Pt(acac) (**1**′), the zero-field splitting is distinctly larger. A value of ΔE(ZFS) = 11.5 cm^{-1} corresponds to a ligand centered triplet state which is moderately perturbed by metal-to-ligand charge transfer (^{1,3}MLCT) admixtures. (dbq)Pt(dpm) (**3**) with ΔE(ZFS) = 46.5 cm^{-1} exhibits a T_1 state with significant MLCT character, the platinum center is distinctly involved in the lowest triplet state. The corresponding ΔE(ZFS) value is the largest one so far reported for monomeric Pt(II) compounds with cyclometalated ligands.

The different magnitudes of the MLCT contributions in the emitting T_1 states clearly manifest themselves in the individual emission decay times of the triplet substates. Corresponding trends are also displayed in the (averaged) decay times of the respective T_1 states at T = 77 K with values of τ(**1**) = 8.7 μs, τ(**2**) = 125 μs, and τ(**3**) = 7.0 μs (Table 2). A comparison of these values with the radiative rates determined at ambient temperature (Table 2) also shows a relatively good correspondence and verifies the trend that k_r(**3**) > k_r(**1**′) ≈ k_r(**1**) ≫ k_r(**2**). (Note that in the subsequent discussion, compounds **1** and **1**′ will be treated equivalently, and thus, the prime will be dropped from now on.)

3.6. Spin−Orbit Coupling Pathways. The results of the high-resolution spectroscopic investigations support the trends obtained at ambient temperature and clearly demonstrate that the efficiency of spin−orbit coupling differs strongly among the studied compounds. The effects of SOC increase in the order **2** ≪ **1** < **3**. For a rationalization of the observed trend, it is instructive to focus on a basic theoretical description of spin−orbit coupling in organo-transition-metal compounds. Both the effects of SOC on the zero-field splitting of the T_1 state and on the radiative rate constants of its substates can be illustrated by formulas based on second order perturbation theory. The energy of one specific triplet substate i of T_1 (with i = I, II, III) can be expressed as[16,66,67,69,83,84]

$$E(i) = E_{T_1} + \sum_{n,j} \frac{|\langle T_n(j)|H_{SO}|T_1(i)\rangle|^2}{E[T_1] - E[T_n]} + \sum_m \frac{|\langle S_m|H_{SO}|T_1(i)\rangle|^2}{E[T_1] - E[S_m]} \quad (1)$$

while the radiative rate constant $k_r(i)$ for the transition from substate i to the singlet ground S_0 state is given by[16,66,67,69,83,85]

$$k_r(i) = \frac{64\pi^4\nu^3}{3hc^3} \cdot \sum_m \left| \frac{\langle S_m|H_{SO}|T_1(i)\rangle}{E[T_1] - E[S_m]} \right|^2 \cdot |\langle S_0|er|S_m\rangle|^2 \quad (2)$$

$E[T_1]$ is the energy of the unperturbed T_1 state, while $E[S_m]$ and $E[T_n]$ represent the energies of higher lying unperturbed singlet states S_m and triplet states T_n. $T_n(j)$ characterizes a substate j of T_n. These (sub)states must have the same symmetry representation as the T_1 substate i; otherwise, the matrix elements in eqs 1 and 2 vanish. H_{SO} is the SOC Hamiltonian, ν and er represent the frequency of the electronic transition energy in s^{-1} and the electric dipole operator, respectively.

It can be seen from the structures of eqs 1 and 2 that SOC matrix elements between a substate of T_1 and higher lying states, as well as energy differences between the respective unperturbed states, determine the amount of energy stabilization of this substate and its radiative rate constant. For the latter quantity, the dipole matrix elements between admixing singlet states S_m and the singlet ground state S_0 are also crucial. Since the SOC matrix elements are usually different for the three T_1 substates, different energy stabilizations are obtained, leading to the zero-field splitting parameters ΔE_{II-I} and ΔE_{III-I}. Equivalently, different radiative rate constants are also a result.

Equations 1 and 2 describe the situation of the so-called direct spin−orbit coupling. This description is valid for a T_1 state of high MLCT character, which couples with other higher lying singlet and triplet MLCT states stemming from a different central metal d orbital.[16,67,69,86] In particular, direct SOC is important for many octahedrally coordinated Ir(III) compounds representing MLCT emitters.[68,83,87] On the other hand, for compounds with emitting triplet states of largely ligand centered (LC) character, direct SOC with ^{1,3}MLCT states is negligibly weak. Instead, a two-step mechanism has to be considered, consisting of configurational mixing (configuration interaction, CI) of the T_1 (^{3}LC) state with a higher lying ^{3}MLCT, which in turn can mix with an adequate ^{1}MLCT state via direct SOC (Figure 9).[67,69,88] In this situation, both CI and SOC matrix elements have to be taken into account, as well as different energy denominators. As a result, this mechanism of state mixing is principally less efficient than the direct SOC paths.

A comparison of the photophysical properties of the different compounds shows that spin−orbit coupling is significantly more efficient in **3** than in **1**. This is evidenced in the total zero-

dx.doi.org/10.1021/ic4011532 | Inorg. Chem. 2013, 52, 12403−12415

field splitting of the T_1 state, which is a factor of 4 greater in the former complex (46.5 cm^{-1} vs 11.5 cm^{-1}). However, the thermally averaged radiative rate constant of **3** is only less than twice as large as that of **1**. On the basis of correlations between ΔE(ZFS) and k_r values from a large number of phosphorescent Os, Ir, and Pt complexes,[16] such a distinct difference in ΔE(ZFS) between **3** and **1** would be expected to induce a more pronounced increase of the radiative rate constant of the former compound. The observed behavior indicates that the most proximate ^{1}MLCT state, which lies distinctly closer to the T_1 state in **3** than in **1** ($\approx$ 2000 vs 3000 cm^{-1}), does not provide significant allowedness to proportionally increase the radiative rate constant of **3**. Thus, it can be concluded that the large ΔE(ZFS) of **3** can be mainly traced back to SOC being effective with higher lying ^{3}MLCT states.

The relatively long emission decay time of the T_1 state (small radiative rate constant) and the very weak intensity of the S_0–T_1 transition in absorption/excitation of compound **2** indicate that spin–orbit coupling of the emitting ^{3}LC state to higher lying singlet states is distinctly less effective for this material than for either **3** or **1**. This difference occurs despite a comparable energy separation (about 3000 cm^{-1}) between the T_1 state and the lowest ^{1}MLCT state of **1** and **2**. Obviously, for compound **2** only the less efficient two-step SOC–CI mechanism, as described above, is responsible for admixing ^{1}MLCT character into the T_1 state. Further, the very small ΔE(ZFS) value also indicates that admixtures of ^{3}MLCT substates to the T_1 substate are unimportant, although a relatively close lying ^{3}MLCT state is observed in the excitation spectrum at 77 K.

4. CONCLUSION

Detailed studies of the complexes **1**–**3** reveal how the luminescent properties are dictated by the triplet characteristics of the respective cyclometalated ppy, bzq, and dbq ligands. Phosphorescence from the complexes originates from a ligand-centered triplet state that is in part (**1** and **3**) strongly perturbed by the metalation to Pt. The complexes have triplet energies that fall in order **3** > **1** > **2**, a sequence that does not correspond to the extent of π-extension in the cyclometalating ligand, nor to the difference in HOMO–LUMO energies of the complexes, but instead follows the trend in the C^N ligand triplet energies. X-ray analysis of the complexes and model C^N ligand precursors show changes in bond lengths promoted by cyclometalation of Pt that parallel intrinsic differences in electronic structures calculated for the triplet state of the unmetalated C^N ligands. Compounds **1** and **3** display similar quinoidal type bond length alterations in their calculated triplet states and thus have similar emission energies, as opposed to the stilbenoid distortions that stabilize the triplet state of **2**. The differences in electronic structure of the C^N ligand in the triplet state also can be used to rationalize variations observed in the radiative rate constants of the complexes (**3** > **1** $\gg$ **2**). These trends follow the same order as values for the ZFS determined using high resolution spectroscopy at low temperatures. However, the ZFS values show variations that are not strictly equivalent to differences in the radiative rate constants. The ZFS of **3** is 4 times larger than that of **1**, whereas the radiative rate constant is only twice as large, despite there also being a smaller energy gap between the lowest singlet MLCT and triplet LC state in **3** than **1**. This behavior shows that spin–orbit coupling in **3** is strongly effective also with higher lying triplet MLCT states. In contrast, the ZFS in **2** is much smaller than that of either **1** or **3**, and the $T_1 \rightarrow S_0$ transition exhibits a correspondingly smaller radiative rate constant. The small ZFS in **2** is a consequence of weak coupling of the emitting triplet state with a higher lying singlet as well as triplet MLCT states. Presumably, this is induced by the stilbenoid distortion in the triplet state of the bzq ligand that shifts electron density away from the Pt center where it is most effective at spin–orbit coupling. These effects reflect the triplet properties of the ligand as described in section 3.3. Electronic redistribution in the T_1 state, along with the accompanied geometrical changes, decreases the electron density at the Pt center where the d-orbitals are most effective at promoting spin–orbit coupling.[16,54] There is an accompanied decrease in electron density at the nitrogen and metalated carbon atoms that directly mediate the spin–orbit coupling. The result of these diminished spin–orbit interactions in **2** is a T_1 state that is almost purely ligand centered.

■ ASSOCIATED CONTENT

Supporting Information

Synthesis of **3′**; ^{1}H NMR spectra for **3′** and **3**; thermal ellipsoid plots for **1**, **1′**, and **2**; CV and DPV traces for **1**, **2**, and **3**; emission spectra for the C^N ligand precursors ppyH, bzqH, and dbqH in 2-methyltetrahydrofuran at 77 K; and X-ray structures for compounds **1**, **1′**, **2**, and **3** in CIF format. This material is available free of charge via the Internet at http://pubs.acs.org.

■ AUTHOR INFORMATION

Corresponding Authors

*E-mail: hartmut.yersin@ur.de.

*E-mail: met@usc.edu.

Notes

The authors declare no competing financial interest.

■ ACKNOWLEDGMENTS

Financial support by the German Federal Ministry of Education and Research (BMBF) and the Universal Display Corporation are gratefully acknowledged. We thank the BaCaTeC and the DAAD for financial support of the exchange program between the University of Regensburg and the University of Southern California. We appreciate NSF CRIF grant 1048807 for the purchase of an X-ray diffractometer.

■ REFERENCES

(1) Williams, J. A. G. *Photochem. Photophys. Coord. Compd. II* **2007**, *281*, 205–268.

(2) Hope, J. M.; Wilson, J. J.; Lippard, S. J. *Dalton Trans.* **2013**, *42*, 3176–3180.

(3) Parker, S. F.; Refson, K.; Bennett, R. D.; Best, J.; Mel'nikov, M. Y.; Weinstein, J. A. *Inorg. Chem.* **2012**, *51*, 9748–9756.

(4) Wu, W. T.; Wu, W. H.; Ji, S. M.; Guo, H. M.; Zhao, J. Z. *Dalton Trans.* **2011**, *40*, 5953–5963.

(5) Wu, W. H.; Sun, J. F.; Ji, S. M.; Wu, W. T.; Zhao, J. Z.; Guo, H. M. *Dalton Trans.* **2011**, *40*, 11550–11561.

(6) Geary, E. A. M.; McCall, K. L.; Turner, A.; Murray, P. R.; McInnes, E. J. L.; Jack, L. A.; Yellowlees, L. J.; Robertson, N. *Dalton Trans.* **2008**, 3701–3708.

(7) Kalinowski, J.; Fattori, V.; Cocchi, M.; Williams, J. A. G. *Coord. Chem. Rev.* **2011**, *255*, 2401–2425.

(8) Che, C. M.; Kwok, C. C.; Lai, S. W.; Rausch, A. F.; Finkenzeller, W. J.; Zhu, N. Y.; Yersin, H. *Chem.—Eur. J.* **2010**, *16*, 233–247.

(9) *Highly Efficient OLEDs with Phosphorescent Materials*; Yersin, H., Ed.; Wiley-VCH: Berlin, 2007.

(10) Kawamura, Y.; Goushi, K.; Brooks, J.; Brown, J. J.; Sasabe, H.; Adachi, C. *Appl. Phys. Lett.* **2005**, *86*, 071104.
(11) Yersin, H. *Top. Curr. Chem.* **2004**, *241*, 1−26.
(12) Anthopoulos, T. D.; Markham, J. P. J.; Namdas, E. B.; Samuel, I. D. W.; Lo, S. C.; Burn, P. L. *Appl. Phys. Lett.* **2003**, *82*, 4824−4826.
(13) Lamansky, S.; Djurovich, P.; Murphy, D.; Abdel-Razzaq, F.; Kwong, R.; Tsyba, I.; Bortz, M.; Mui, B.; Bau, R.; Thompson, M. E. *Inorg. Chem.* **2001**, *40*, 1704−1711.
(14) Lamansky, S.; Djurovich, P.; Murphy, D.; Abdel-Razzaq, F.; Lee, H. E.; Adachi, C.; Burrows, P. E.; Forrest, S. R.; Thompson, M. E. J. *Am. Chem. Soc.* **2001**, *123*, 4304−4312.
(15) Baldo, M. A.; O'Brien, D. F.; You, Y.; Shoustikov, A.; Sibley, S.; Thompson, M. E.; Forrest, S. R. *Nature* **1998**, *395*, 151−154.
(16) Yersin, H.; Rausch, A. F.; Czerwieniec, R.; Hofbeck, T.; Fischer, T. *Coord. Chem. Rev.* **2011**, *255*, 2622−2652.
(17) Thompson, M. E.; Djurovich, P. I.; Barlow, S.; Marder, S. R. In *Comprehensive Organometallic Chemistry*; O'Hare, D., Ed.; Elsevier: Oxford, U. K., 2007; Vol. *12*, pp 101−194.
(18) Djurovich, P. I.; Murphy, D.; Thompson, M. E.; Hernandez, B.; Gao, R.; Hunt, P. L.; Selke, M. *Dalton Trans.* **2007**, 3763−3770.
(19) Brooks, J.; Babayan, Y.; Lamansky, S.; Djurovich, P. I.; Tsyba, I.; Bau, R.; Thompson, M. E. *Inorg. Chem.* **2002**, *41*, 3055−3066.
(20) Fornies, J.; Fuertes, S.; Lopez, J. A.; Martin, A.; Sicilia, V. *Inorg. Chem.* **2008**, *47*, 7166−7176.
(21) Jolliet, P.; Gianini, M.; von Zelewsky, A.; Bernardinelli, G.; Stoeckli-Evans, H. *Inorg. Chem.* **1996**, *35*, 4883−4888.
(22) Ruziewicz, Z.; Gluchows, H. *Bull. Acad. Pol. Sci., Ser. Sci., Math., Astron. Phys.* **1968**, *16*, 153−159.
(23) Maestri, M.; Sandrini, D.; Balzani, V.; Maeder, U.; Von Zelewsky, A. *Inorg. Chem.* **1987**, *26*, 1323−1327.
(24) Miki, H.; Azumi, T. *J. Phys. Chem.* **1994**, *98*, 6059−6062.
(25) Murov, S. L.; Carmichael, I.; Hug, G. L. *Handbook of Photochemistry*, 2nd ed.; Marcel Dekker: New York, 1993.
(26) Cho, J. Y.; Suponitsky, K. Y.; Li, J.; Timofeeva, T. V.; Barlow, S.; Marder, S. R. J. *Organomet. Chem.* **2005**, *690*, 4090−4093.
(27) Pavlishchuk, V. V.; Addison, A. W. *Inorg. Chim. Acta* **2000**, *298*, 97−102.
(28) Gagne, R. R.; Koval, C. A.; Lisensky, G. C. *Inorg. Chem.* **1980**, *19*, 2854−2855.
(29) Frisch, M. J.; Trucks, G. W.; Schlegel, H. B.; Scuseria, G. E.; Robb, M. A.; Cheeseman, J. R.; Montgomery, J. A., Jr.; Vreven, T.; Kudin, K. N.; Burant, J. C.; Millam, J. M.; Iyengar, S. S.; Tomasi, J.; Barone, V.; Mennucci, B.; Cossi, M.; Scalmani, G.; Rega, N.; Petersson, G. A.; Nakatsuji, H.; Hada, M.; Ehara, M.; Toyota, K.; Fukuda, R.; Hasegawa, J.; Ishida, M.; Nakajima, T.; Honda, Y.; Kitao, O.; Nakai, H.; Klene, M.; Li, X.; Knox, J. E.; Hratchian, H. P.; Cross, J. B.; Adamo, C.; Jaramillo, J.; Gomperts, R.; Stratmann, R. E.; Yazyev, O.; Austin, A. J.; Cammi, R.; Pomelli, C.; Ochterski, J. W.; Ayala, P. Y.; Morokuma, K.; Voth, G. A.; Salvador, P.; Dannenberg, J. J.; Zakrzewski, V. G.; Dapprich, S.; Daniels, A. D.; Strain, M. C.; Farkas, O.; Malick, D. K.; Rabuck, A. D.; Raghavachari, K.; Foresman, J. B.; Ortiz, J. V.; Cui, Q.; Baboul, A. G.; Clifford, S.; Cioslowski, J.; Stefanov, B. B.; Liu, G.; Liashenko, A.; Piskorz, P.; Komaromi, I.; Martin, R. L.; Fox, D. J.; Keith, T.; Al-Laham, M. A.; Peng, C. Y.; Nanayakkara, A.; Challacombe, M.; Gill, P. M. W.; Johnson, B.; Chen, W.; Wong, M. W.; Gonzalez, C.; Pople, J. A. *Gaussian 03*; Gaussian, Inc.: Wallingford, CT, 2004.
(30) *SMART*; Bruker Analytical X-ray System, Inc.: Madison, WI, 2001.
(31) *SAINT*; Bruker Analytical X-ray System, Inc.: Madison, WI, 2001.
(32) *SAINT-Plus*; Bruker Analytical X-ray System, Inc.: Madison, WI, 2005.
(33) *SHELXTL*; Bruker Analytical X-ray System, Inc.: Madison, WI, 1997.
(34) *SHELXTL*; Bruker Analytical X-ray System, Inc.: Madison, WI, 2002.
(35) *SHELXL-97*; Bruker Analytical X-ray System, Inc.: Madison, WI, 1997.
(36) Sheldrick, G. M.; Schneider, T. R.; Carter, C. W. J.; Sweet, R. M. In *Methods Enzymol.*; Academic Press: New York, 1997; Vol. *277*, pp 319−343.
(37) *SHELXL-2012-4*; Bruker Analytical X-ray System, Inc.: Madison, WI, 2012.
(38) *SADABS*; Bruker Analytical X-ray System, Inc.: Madison, WI, 2001.
(39) Blessing, R. H. *Acta Crystallogr., Sect. A* **1995**, *51*, 33−38.
(40) Chassot, L.; Muller, E.; Von Zelewsky, A. *Inorg. Chem.* **1984**, *23*, 4249−4253.
(41) Ghedini, M.; Pucci, D.; Crispini, A.; Barberio, G. *Organometallics* **1999**, *18*, 2116−2124.
(42) Stoccoro, S.; Alesso, G.; Cinellu, M. A.; Minghetti, G.; Zucca, A.; Manassero, M.; Manassero, C. *Dalton Trans.* **2009**, 3467−3477.
(43) Esteruelas, M. A.; Fernandez-Alvarez, F. J.; Olivan, M.; Onate, E. *Organometallics* **2009**, *28*, 2276−2284.
(44) Andreetti, G. D.; Lipkowski, J. *Cryst. Struct. Comm.* **1981**, *10*, 1211−1215.
(45) Ghedini, M.; Pugliese, T.; La Deda, M.; Godbert, N.; Aiello, I.; Amati, M.; Belviso, S.; Lelj, F.; Accorsi, G.; Barigelletti, F. *Dalton Trans.* **2008**, 4303−4318.
(46) Jude, H.; Bauer, J. A. K.; Connick, W. B. *J. Am. Chem. Soc.* **2003**, *125*, 3446−3447.
(47) Kvam, P. I.; Puzyk, M. V.; Balashev, K. P.; Songstad, J. *Acta Chem. Scand.* **1995**, *49*, 335−343.
(48) Pabst, M.; Sundholm, D.; Koehn, A. *J. Phys. Chem. C* **2012**, *116*, 15203−15217.
(49) Vlcek, A., Jr.; Zalis, S. *Coord. Chem. Rev.* **2007**, *251*, 258−287.
(50) Dobbs, K. D.; Sohlberg, K. *J. Chem. Theory Comput.* **2006**, *2*, 1530−1537.
(51) Baird, N. C. *J. Am. Chem. Soc.* **1972**, *94*, 4941−4948.
(52) Hanson, K.; Roskop, L.; Djurovich, P. I.; Zahariev, F.; Gordon, M. S.; Thompson, M. E. *J. Am. Chem. Soc.* **2010**, *132*, 16247−16255.
(53) Mou, X.; Wu, Y. Q.; Liu, S. J.; Shi, M.; Liu, X. M.; Wang, C. M.; Sun, S.; Zhao, Q.; Zhou, X. H.; Huang, W. *J. Mater. Chem.* **2011**, *21*, 13951−13962.
(54) Bakova, R.; Chergui, M.; Daniel, C.; Vlcek, A., Jr.; Zalis, S. *Coord. Chem. Rev.* **2011**, *255*, 975−989.
(55) Baunsgaard, D.; Harrit, N.; El Balsami, M.; Negri, F.; Orlandi, G.; Frederiksen, J.; Wilbrandt, R. *J. Phys. Chem. A* **1998**, *102*, 10007−10016.
(56) Kanda, Y.; Shimada, R.; Sakai, Y. *Spectrochim. Acta* **1961**, *17*, 1−6.
(57) Kanda, Y.; Shimada, R. *Spectrochim. Acta* **1959**, *15*, 211−224.
(58) Caspar, J. V.; Meyer, T. J. *J. Phys. Chem.* **1983**, *87*, 952−957.
(59) Englman, R.; Jortner, J. *Mol. Phys.* **1970**, *18*, 145−164.
(60) Sajoto, T.; Djurovich, P. I.; Tamayo, A. B.; Oxgaard, J.; Goddard, W. A.; Thompson, M. E. *J. Am. Chem. Soc.* **2009**, *131*, 9813−9822.
(61) Yang, L.; Okuda, F.; Kobayashi, K.; Nozaki, K.; Tanabe, Y.; Ishii, Y.; Haga, M. A. *Inorg. Chem.* **2008**, *47*, 7154−7165.
(62) Maruszewski, K.; Strommen, D. P.; Kincaid, J. R. *J. Am. Chem. Soc.* **1993**, *115*, 8345−8350.
(63) Danielson, E.; Lumpkin, R. S.; Meyer, T. J. *J. Phys. Chem.* **1987**, *91*, 1305−1306.
(64) Thompson, D. W.; Fleming, C. N.; Myron, B. D.; Meyer, T. J. *J. Phys. Chem. B* **2007**, *111*, 6930−6941.
(65) Turro, N. J. *Modern Molecular Photochemistry*; Benjamin/Cummings: Menlo Park, CA, 1978.
(66) McGlynn, S. P.; Azumi, T.; Kinoshita, M. *Molecular Spectroscopy of the Triplet State*; Prentice Hall: Englewood Cliffs, NJ, 1969.
(67) Rausch, A. F.; Homeier, H. H. H.; Yersin, H. *Top. Organomet. Chem.* **2010**, *29*, 193−235.
(68) Hofbeck, T.; Yersin, H. *Inorg. Chem.* **2010**, *49*, 9290−9299.
(69) Rausch, A. F.; Homeier, H. H. H.; Djurovich, P. I.; Thompson, M. E.; Yersin, H. *Org. Light Emitting Mater. Devices XI* **2007**, *6655*, F6550−F6550.
(70) Yersin, H.; Humbs, W.; Strasser, J. *Top. Curr. Chem.* **1997**, *191*, 153−249.

(71) Shpol'skii, E. V. *Sov. Phys. Usp. (Engl. Transl.)* **1960**, *3*, 372.
(72) Rausch, A. F.; Thompson, M. E.; Yersin, H. *Chem. Phys. Lett.* **2009**, *468*, 46−51.
(73) Rausch, A. F.; Murphy, L.; Williams, J. A. G.; Yersin, H. *Inorg. Chem.* **2009**, *48*, 11407−11414.
(74) Yersin, H.; Donges, D. *Top. Curr. Chem.* **2001**, *214*, 81−186.
(75) Rausch, A. F. *Diplomarbeit*; Universität Regensburg: Regensburg, Germany, 2006.
(76) Rausch, A. F.; Yersin, H. *Chem. Phys. Lett.* **2010**, *484*, 261−265.
(77) Huber, R. *Diplomarbeit*; Universität Regensburg: Regensburg, Germany, 2008.
(78) Finkenzeller, W. J.; Stossel, P.; Yersin, H. *Chem. Phys. Lett.* **2004**, *397*, 289−295.
(79) Finkenzeller, W. J.; Yersin, H. *Chem. Phys. Lett.* **2003**, *377*, 299−305.
(80) Harrigan, R. W.; Crosby, G. A. *J. Chem. Phys.* **1973**, *59*, 3468−3476.
(81) Tinti, D. S.; El-Sayed, M. A. *J. Chem. Phys.* **1971**, *54*, 2529−2549.
(82) Azumi, T.; Odonnell, C. M.; McGlynn, S. P. *J. Chem. Phys.* **1966**, *45*, 2735−2742.
(83) Yersin, H.; Rausch, A. F.; Cerwieniec, R. In *Physics of Organic Semiconductors*; Bruetting, W., Adachi, C., Eds.; Wiley-VCH: Weinheim, Germany, 2012; p 371.
(84) Ikeda, S.; Yamamoto, S.; Nozaki, K.; Ikeyama, T.; Azumi, T.; Burt, J. A.; Crosby, G. A. *J. Phys. Chem.* **1991**, *95*, 8538−8541.
(85) Abedin-Siddique, Z.; Ohno, T.; Nozaki, K. *Inorg. Chem.* **2004**, *43*, 663−673.
(86) Obara, S.; Itabashi, M.; Okuda, F.; Tamaki, S.; Tanabe, Y.; Ishii, Y.; Nozaki, K.; Haga, M. *Inorg. Chem.* **2006**, *45*, 8907−8921.
(87) Rausch, A. F.; Thompson, M. E.; Yersin, H. *J. Phys. Chem. A* **2009**, *113*, 5927−5932.
(88) Miki, H.; Shimada, M.; Azumi, T.; Brozik, J. A.; Crosby, G. A. *J. Phys. Chem.* **1993**, *97*, 11175−11179.

■ NOTE ADDED AFTER ASAP PUBLICATION

After this paper was published ASAP on October 11, 2013, several corrections were made to the text. The corrected version was reposted October 24, 2013.